coatings

MDPI

Article

Design, Simulation and Performance Research of New Biomaterial $Mg_{30}Zn_{30}Sn_{30}Sr_5Bi_5$

Beiyi Ma *, Dongying Ju * and Qian Liu *

School of Mechanical Engineering and Automation, University of Science and Technology Liaoning, Anshan 114051, China

* Correspondence: mbeiy@126.com (B.M.); jdy_20220224@126.com (D.J.); tclan1987@163.com (Q.L.)

Abstract: This study focused on the design and the preparation method of a new biomaterial, $Mg_{30}Zn_{30}Sn_{30}Sr_5Bi_5$ (at%) alloy, and its simulation and property analyses. Based on the comprehensive consideration of the preparation of high-entropy alloys, the selection of biomaterial elements, and the existing research results of common Mg-based materials, the atomic percentage of various elements, that is, Mg:Zn:Sn:Sr:Bi = 30:30:30:5:5, was determined. Using the theoretical methods of thermodynamic performance analysis and solidification performance analysis, the proposed composition was simulated and analyzed. The analysis results showed that the mechanical properties of the new material can meet the design requirements, and it can be prepared in physical form. XRD, SEM, PSD, compression tests, and other experimental tests were conducted on the material, and the alloy composition and distribution law showed various characteristics, which conformed to the "chaotic" characteristics of high-entropy alloys. The elastic modulus of the material was 17.98 GPa, which is within the 0–20 GPa elastic modulus range of human bone. This means that it can avoid the occurrence of stress shielding problems more effectively during the material implantation process.

Keywords: Mg-based alloy; biomaterials; high-entropy alloys; $Mg_{30}Zn_{30}Sn_{30}Sr_5Bi_5$ (at%) alloy; stress shielding; elastic modulus

Citation: Ma, B.; Ju, D.; Liu, Q. Design, Simulation and Performance Research of New Biomaterial $Mg_{30}Zn_{30}Sn_{30}Sr_5Bi_5$. *Coatings* **2022**, *12*, 531. https://doi.org/10.3390/coatings12040531

Academic Editors: Devis Bellucci and Anton Ficai

Received: 24 February 2022
Accepted: 12 April 2022
Published: 14 April 2022

1. Introduction

Biological materials refer to natural or man-made materials that can be applied in the diagnosis, treatment, and recovery of diseased or damaged organic tissues or organs without adverse effects on biological organisms [1]. At present, many universally acknowledged biomaterials exist, such as stainless steel, Co-based alloys, Ti and Ti-based alloys, and Mg-based alloys. They all exhibit excellent mechanical properties, such as high strength, good malleability, favorable processing capacity, and outstanding corrosion stability. Numerous research results exist on biomaterials. High-nitrogen nickel-free austenitic steel Fe-21Cr-22Mn-1Mo-1N as a biomaterial is included in ASTM [2]. In The General Technological Conditions of Surgical Metal Implant (GB), Fe-21Cr-22Mn-1Mo-1N and super-low carbon stainless steel Cr-Ni-Mo have the same medical properties. Co-based alloys, F76, F90, F562, F563, etc., are recommended as surgical implants by ASTM. Pure titanium (Ti) and, currently, some of the titanium-based alloys, are among the most attractive metallic materials for biomedical applications (as implants) due to their non-biodegradability, good mechanical properties, and good biocompatibility [3]; for example, Ti-35Nb-5Ta-7Zr by Prof. H. J. Rack of Celmson University [4], Ti-29Nb-13Ta-5Zr by Prof. M. Niinomi of Toyohashi University of Technology [5], and TLE alloy and TLM alloy by Northwest Institute for Non-ferrous Metal Research China [6] are recommended for surgical implants.

Mg and Mg-based alloy have become a research focus in the field of biomedical applications because of their low density, high specific strength, low Young's modulus [7–12], superior bio-compatibility, and bio-degradation [13,14]. The research on the medical properties of Mg-based alloys has continuously advanced; for example, Zberg B. et al. found that amorphous

Mg-Zn alloy with Zn content of 50% is a promising biomaterial [15], and Mg66Zn30Ca4 by Prof. Y. F. Zheng, etc. of School of Materials Science and Engineering, Peking University [16]. Mg-based biomaterials, as a kind of biological implant material with excellent performance, have been widely used in the medical field. Witte et al. studied the implantation behavior of Mg-based alloys, AZ31, AZ91, LAE442, and WE43 [17]. Waizy et al. [18], Dickmann et al. [19], and Windhagen [20] et al. conducted clinical research on MgYREZr alloy. Kenan et al. developed a Mg-5Ca-1Zn screw for internal fixation of palm fractures [21]. Compression screws made of a biodegradable Mg-based alloy, MgYREZr, were developed by Syntellix AG, Germany. The Mg-Ca screws manufactured by U&I Company were approved by Korea MFDS for joint fracture fixation.

The elastic modulus of existing Mg-based biomaterials is in the range of 41–45 GPa (for example, that of AZ31B, AZ91D, AM60B, AM50A, and Pure Mg are 45 GPa, that of Mg-3Al-4Zn-0.2Ca is 44.1 GPa, and that of Mg-4Al-4Zn-0.2Ca is 45 GPa, et al.), whereas the elastic modulus of human bones is in the range of 3–20 GPa (for example, cancellous bone: 3.0~14.8 GPa; os hamatum integumentale: 18.6~7.0 Gpa; dentin: 15 GPa, et al.) [22]. The difference in elastic modulus causes the phenomenon of "stress shielding" in implant materials [23]. Stress-shielding effects arise from shear stresses due to the difference in material properties between bone and the implant [24]. The main purpose of this research was to use the methods applied in the study of high-entropy alloys to design and prepare Mg-based biomaterials. The utilized characteristics, which are the multi-element and multi-component characteristics of high-entropy alloys, modify the elastic modulus of the material by adjusting the atomic percentage of the element of the new material. Thus, the elastic modulus of the new material is numerically closer to that of human bone. This can avoid the stress shielding caused by the difference in elastic moduli, ensuring human bone can be repaired and grown [25].

2. Element Selection Basis

2.1. The Principles of High-Entropy Alloy and Biomaterial Design

The main purpose of the section is to present the determination of the element composition of the new Mg-based biomaterial. Its elements were chosen to consider three main factors. First, the definition of high-entropy alloys (HEAs) is that they must contain at least five principal elements having an atomic percentage between 5% and 35% [26–28]. For better formation of solid solution phases in high-entropy alloys, an atomic size difference $\leq$6.6% has been suggested [29,30]. Second, according to the published papers and results of research, a large number of elements have been used in the preparation of various high-entropy alloys, such as, AlCoCrCu FeNi [31], RhIrPdPtNiCu [32], (Ag/In/Cd/Sn/Sb/Pb/Bi)-Te [33], AlCrFeCoNiZn [34], (Al/Cr/V/Sn)NbTaTiZr [35], MgAlSiCrFe [36], and MgAlLiZn-CaY/MgAlLiZnCaCu [37]. Third, in recent years, a great deal of research has been conducted on various biomaterials, particularly Mg-based biomaterials, and many elements, including Mg, Zn, Ca, Mn, Nb, Sn, Sr, Bi, Li, Gd, Zr, and Ti [38–42], have appeared in the selection of Mg-based biomaterials. To summarize, the composition of the Mg-based high-entropy biomaterial is Mg30Zn30Sn30 Sr5Bi5 (at.%). All of the elements that compose the Mg-based high-entropy biomaterial have better biological properties. Mg, Zn, and Sn are important elements of the human body, and ensure basic safety for biomedical applications. Mg is an essential element in human bone tissues, and is beneficial to the strength and growth of bone. Regarding Zn, 60% in the human body exists in the muscle and 30% exists in the bone tissues; it is also a component of many enzymes, which help the synthesis of proteins and DNA, and promote cell regeneration and tissue metabolism. The main physiological function of Sn is in anti-tumor activity by inhibiting the formation of cancer cells; it can also promote the synthesis of proteins and nucleic acids, and enhance the stability of the body environment [43,44]. Sr is chemically and physically similar to calcium, and can be used to treat osteoporosis because it can stimulate bone formation and inhibit bone resorption [45]. Bi is called a 'Green Metal' because it is nontoxic to the human body, and can be used to treat gastrointestinal and dyspepsia in the

form of compounds, such as Bismuth Subcarbonate and Bismuth Subnitrate, and is used as an additive for cosmetics [46].

2.2. The Influence of Elements on Mg Alloys

Bi is an element with a precipitation strengthening effect in Mg. After its addition, it can form a Mg3Bi2 term with better thermal stability, so as to achieve the refinement of the as-cast microstructure and help improve the room temperature mechanical properties of Mg alloys [47]. After Sn is added to pure magnesium, the coarse columnar crystal ingot can be transformed into an equiaxed crystal, and the crystal grain can be refined, and the Mg_2Sn phase with cubic C1 structure characteristics can be generated in the structure [48]. The maximum solid solubility of Sn at 561.2 °C is 14.85%. When the temperature drops to 200 °C, the alloy solid solubility is almost zero. The precipitated Mg2Sn eutectic phase can form a dispersion-strengthened structure. Like Al, Zn not only has a solid solution strengthening effect in Mg, but also has an aging strengthening effect. Zn can weaken the adverse effects of some impurities in the alloy (such as iron and nickel) on its corrosion resistance. Zn can also reduce the end temperature of Mg alloy solidification. The addition of the Sr element can refine the grains of Mg alloy to reduce the tendency of microporosity and hot cracking, and improve Mg alloy's die-casting performance and mechanical properties [49].

3. Performance Simulation

3.1. Theoretical Basis

Based on the fact that there are many uncontrollable factors in the research of new materials, the simulation calculation of related properties was carried out using the CALPHAD Technology, which is well developed at present; therefore, the feasibility of the research was confirmed. The research mainly focused on thermodynamic properties, and solidification phases and properties. The theoretical formulas include the thermodynamic principles, the Scheil–Gulliver Model, and the calculation of material properties.

According to the thermodynamic principles, the general conditions for the system to reach equilibrium under constant pressure are as follows:

A. Assuming G (Total Gibbs Free Energy) of the system reaches the minimum value G min, the chemical potentials of each component *i* are equal. Equation (1) is the molar Gibbs Free Energy of each term.

$$G_m = \sum_i X_i G_i^0 + RX \sum_i X_i \ln X_i + \sum_i \sum_j X_i X_j \sum_v \Omega_i \left(X_i - X_j\right)^v, \quad \begin{bmatrix} \frac{\partial G_m(\alpha)}{\partial X_i} = \frac{\partial G_m(\beta)}{\partial X_i} \\ \mu_i(\alpha) = \mu_i(\beta) \end{bmatrix} \tag{1}$$

B. Assuming the solute diffusion in the solid phase can be ignored, and the solute in the liquid phase diffuses rapidly and completely, Equation (2) calculates the alloy composition in the solid phase. Equation (3) calculates the fraction of solid formed.

$$C_S = kC_0(1 - f_s)^{k-1} \tag{2}$$

$$f_s = 1 - \left(\frac{T_f - T}{T_f - T_L}\right)^{\left[\frac{1}{k-1}\right]} \tag{3}$$

C. Assuming that non-equilibrium conditions are met, Equation (4) calculates the relative properties of each phase based on the alloy composition of each phase. Equation (5) calculates the overall properties of the material according to the law of mixing.

$$P = \sum_i x_i P_i^0 + \sum_i \sum_{j>1} x_i y_i \left(\sum_v \Omega_{ij}^v \left(x_i - y_j\right)^v\right) \tag{4}$$

$$P_t = x_\alpha P_\alpha + x_\beta P_\beta + P_{III} F_s \quad (5)$$

3.2. Simulation Conditions

The conditions of simulation included the following: the atomic percentage of the elements was Mg:Zn:Sn:Sr:Bi = 30:30:30:5:5 (at.%); the simulated temperature range was set as 1000–25 °C; the step size was 20; the initial cooling rate was 1000 C/s; and Mg was used as the equilibrium reference for simulation analysis. The simulation consisted of thermodynamic analysis and solidification analysis.

3.3. Simulation Results and Analysis

The simulation included thermodynamic analysis and solidification analysis.

The data obtained through simulation were analyzed from two perspectives according to the theories of high entropy alloys and biomaterials. As shown in Figure 1, the density value of the alloy in this study is about 6.20 g/cm^3, and the volume change rate is 12.14%. This value is in the middle of the range of common metallic biomaterials, and is higher than that of Mg alloy (1.74–2.0 g/cm^3) and Ti alloy (4.4–4.5 g/cm^3), but lower than that Co-Cr alloy (8.3–9.2 g/cm^3) and stainless steel (7.9–8.1 g/cm^3). However, this density value only applies to one atomic ratio condition. The minimum density is 3.76 g/cm^3 after changing the atomic percentage, which is calculated by the exhaustive method. This is more in line with the demand of biomaterials for Mg-based materials.

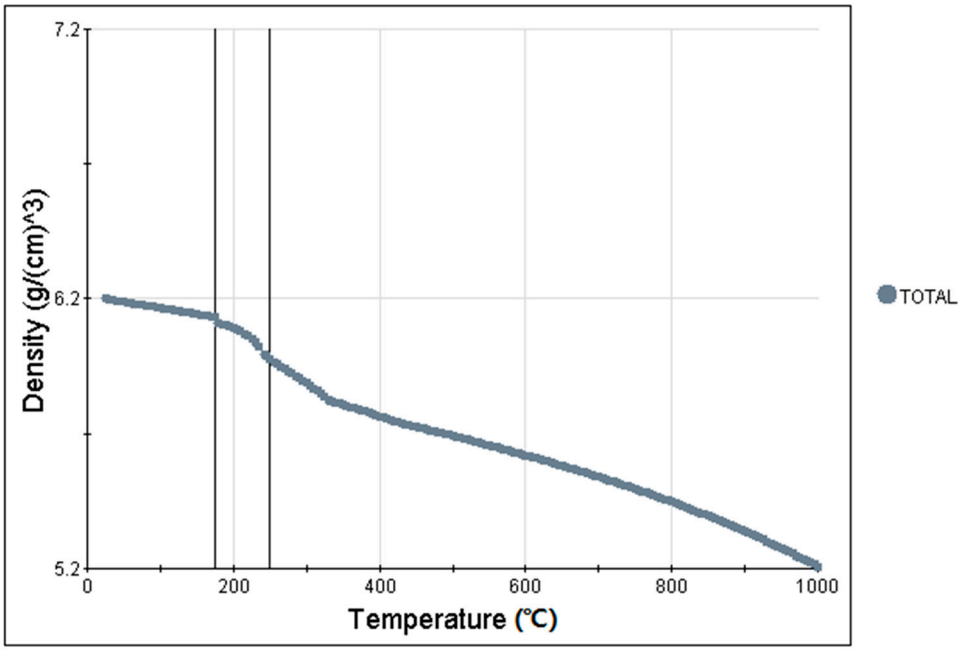

Figure 1. Results of analysis of solidification phases and properties: density (g/cm^{-3})—temperature (°C).

Combined with the heat capacity–temperature curve and data analysis, as shown in Figure 2, Sn solid solution precipitates in the alloy at 89.75 °C. The obvious peak structure appears at 230–250 °C. The peak appears at 232.43 °C, and the HCmax is 266.02 J/(mole K), which indicates that the material produced a solid–liquid phase transition in this interval. MgZn2 precipitates at 333.36 °C, and Mg2X-C1 precipitates at 420.57 °C.

The spacing–initial cooling rate curve from the analysis of solidification phases and properties suggests that, as shown in Figure 3, the spacing decreases with the increase in the initial cooling rate; in particular, in the range of 0–1 °C/s, the spacing decreases sharply. In the range from 1 to 10 °C/s, the spacing decreases rapidly. However, above 10 °C/s, the spacing does not change significantly. The tensile stress, 0.2% proof strength, and hardness change in

the same way as spacing, as shown in Figure 4. In the range of 0–1–10–100 °C/s, the spacing varies in the range of 104.06–61.18–28.62–13.39 μm. In the range of 1–10–100 °C/s, the tensile stress value varies in the range of 478.93–748.28–1221.79 MPa, the 0.2% proof stress varies in the range of 359.84–661.73–1194.64 MPa, and the hardness range is 4.89–0.37–40.19 HRC.

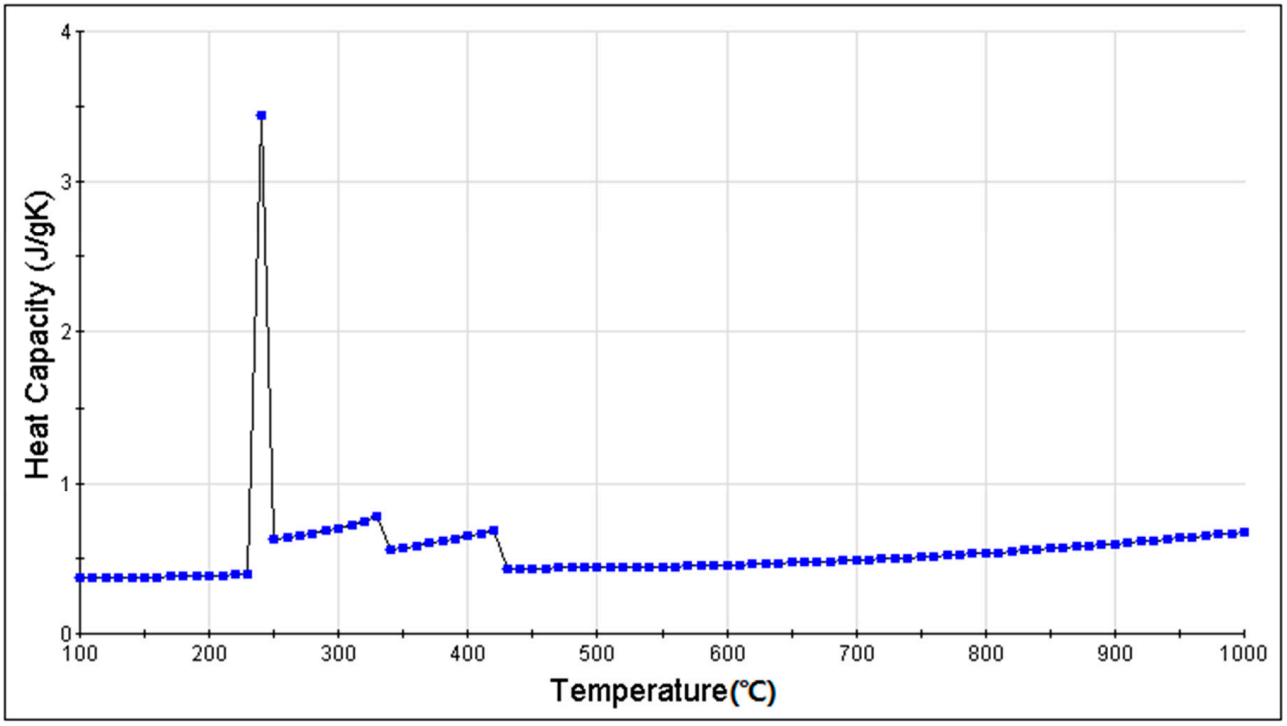

Figure 2. Results of analysis of solidification phases and properties: heat capacity (J/(mole K))–temperature (°C).

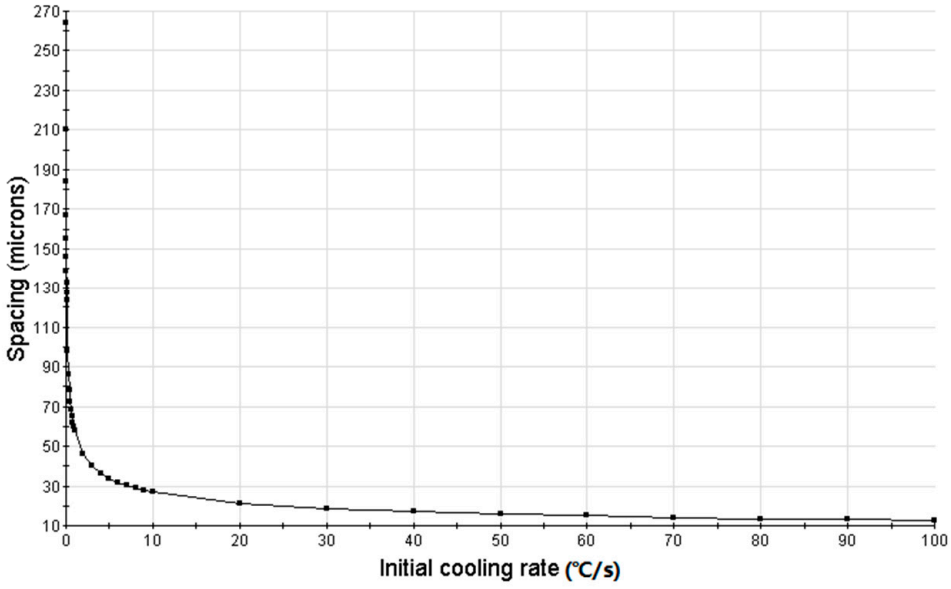

(**a**)

Figure 3. *Cont.*

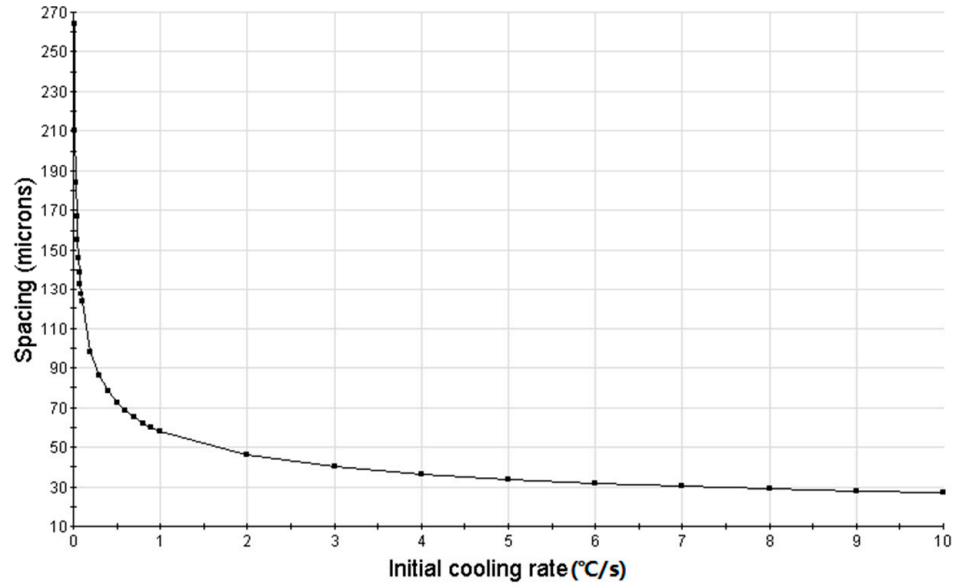

(**b**)

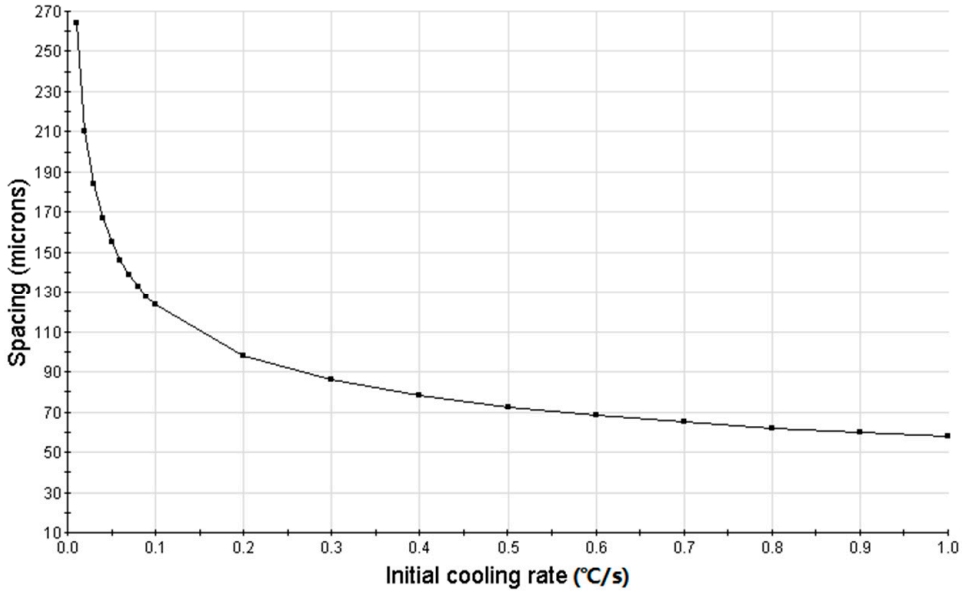

(**c**)

Figure 3. Result of analysis of solidification phases and properties: spacing (microns)–initial cooling rate (°C/s): (**a**) initial cooling rate 100 °C/s; (**b**) initial cooling rate 10 °C/s; (**c**) initial cooling rate 1 °C/s.

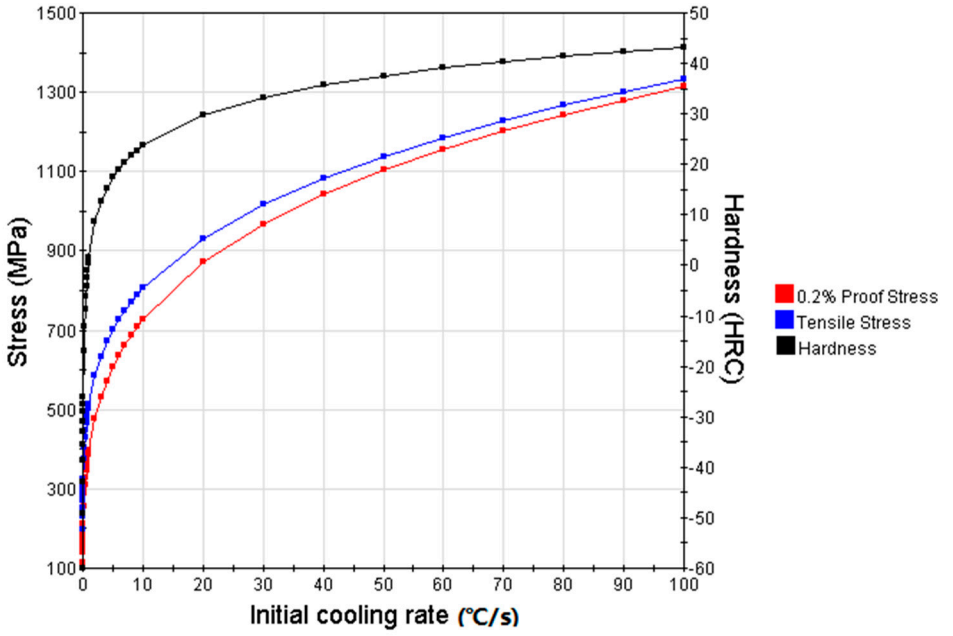

(**a**)

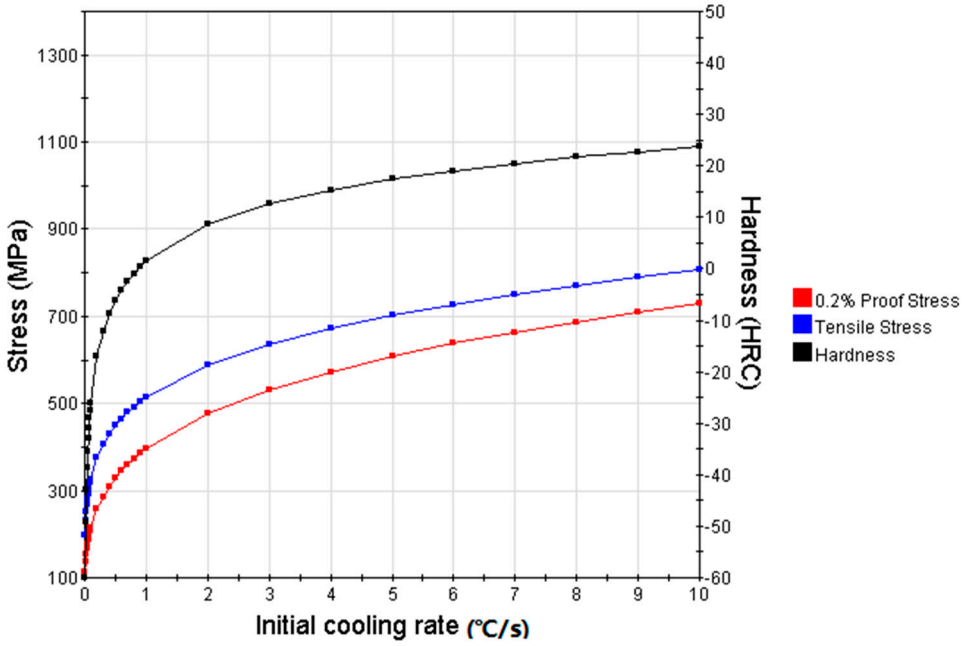

(**b**)

Figure 4. *Cont.*

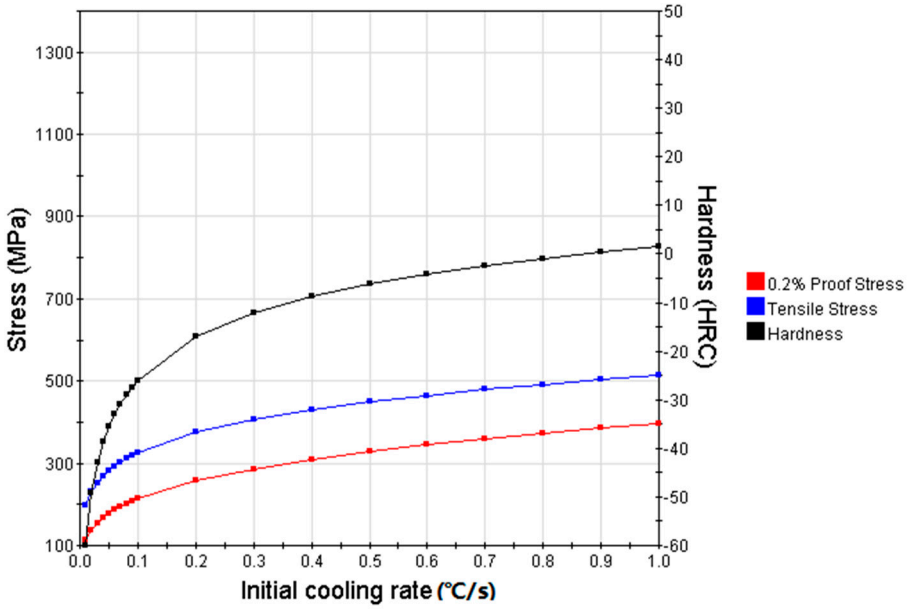

(**c**)

Figure 4. Result of analysis of solidification phases and properties: tensile stress (MPa)/0.2% proof stress (MPa)/hardness (HRC)–initial cooling rate (°C/s): (**a**) initial cooling rate 100 °C/s; (**b**) initial cooling rate 10 °C/s; (**c**) initial cooling rate 1 °C/s.

According to the Young's modulus–temperature curve, as shown in Figure 5, the Young's modulus is 56.09 GPa when the liquid–solid transition completes.

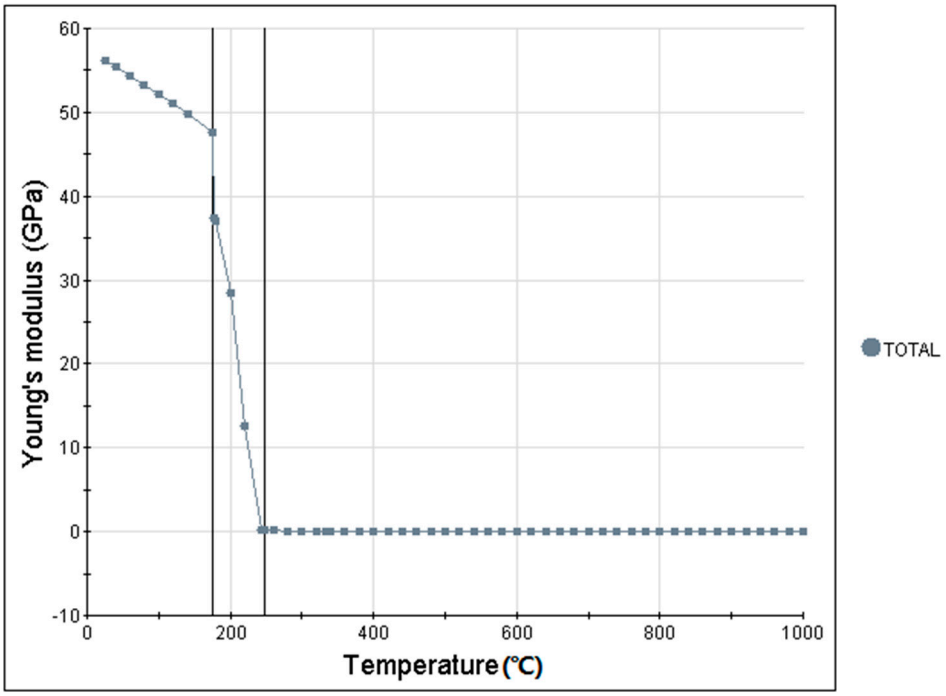

Figure 5. Result of analysis of solidification phases and properties: Young's modulus (GPa)–temperature °C.

All the analysis results above, combined with the production technology, material performance requirements, and other factors, have important reference value for material preparation conditions.

4. Preparation Method

4.1. As-Cast Alloy Preparation

The $Mg_{30}Zn_{30}Sn_{30}Sr_5Bi_5$ at.% alloy is prepared in a vacuum high-frequency melting furnace with a mild steel crucible protected by argon gas. To prepare the alloys, the following are added: pure Mg (Granules, purity 99.99 wt.%, specification model is Ø4 × 4 mm), pure Zn (Granules, purity 99.999 wt.%, specification model is 1–3 mm), pure Sn (Granules, purity 99.999 wt.%, specification model is 1–6 mm), pure Sr (Granules, purity 99.9 wt.%, specification model is 1–3 cm), pure Bi (Granules, purity 99.999 wt.%, specification model is 1–3 mm). Before use, the mild steel crucible needs to be cleaned to remove impurities, and dried. All materials need to have grease and oxide layers removed. These operations need to be completed in a sealed box to reduce the oxidation problem. After the prepared material is place into the vacuum high-frequency melting furnace, the mechanical pump is turned on, the pressure in the furnace is reduced to the standard value (6×10^{-3} Pa) by vacuum, and the furnace is then filled with argon protective gas. Finally, the pressure in the furnace is 0.05 MPa. The smelting process needs to be completed in a furnace filled with argon, and the heating rate is 0.5 °C/s. In order to ensure the material melting effect during the heating process, the melting of the material in the crucible must be able to be monitored at any time through the furnace body observation window, and a stirring rod must be used as needed to ensure that the material is fully dissolved. The maximum heating temperature for smelting is 700–750 °C, and this needs to be maintained for 30 min after reaching the melting temperature. After the metal material is completely melted, the stirrer is turned on again to fully stir for 5 min. After stirring, the material is maintained at 700–750 °C, for 60 min. The whole preparation process must not only ensure complete argon protection conditions during the smelting process, but after the metal material smelting process is completed, the material must also be cooled and solidified naturally in the furnace under the action of the argon protection gas. Finally, an irregular block material is obtained, as the picture shows.

$Mg_{30}Zn_{30}Sn_{30}Sr_5Bi_5$ at.% alloy ingots were prepared as shown in Figure 6.

Figure 6. $Mg_{30}Zn_{30}Sn_{30}Sr_5Bi_5$ (at%) alloy block (40 mm × 40 mm × 20 mm).

4.2. Experimental Preparation

New material performance test experiments included SEM, XRD, PSD, and the compression test. The specimens are obtained by wire cutting.

The XRD pattern was obtained using a Cu-Kα lamp with wavelength λ = 1/5406 Å in the range $0 < 2\theta < 90°$, step 0.02, and 1 s time for each step. Then, the XRD analysis was performed by comparing the angle and intensity of the diffraction peaks with the informa-

tion in the standard cards. The microstructure, particle distribution, and morphology of $Mg_{30}Zn_{30}Sn_{30}Sr_5Bi_5$ (at.%) were investigated using a Gemini 300 SEM. The samples were coated with a very thin layer of gold to increase the electrical conductivity of the specimen surface and to enhance the clarity of the images [50,51]. The PSD test was conducted using a Setaram Setsys Evo Simultaneous thermal analyzer.

All specimens are shown in Figure 7.

(**a**) (**b**) (**c**)

Figure 7. The experimental specimens. (**a**) 10 mm × 10 mm × 3 mm. Specimen used for SEM (Gemini 300 scanning electron microscope), XRD (X' Pert Powder diffractometer), and hardness testing (HV-1000 microhardness tester). Specimen was polished and inlaid with resin. Initial cooling rate 100 °C/s. (**b**) Specimen used for compressive testing (WDW-100 electronic universal tester). (**c**) Specimen used for PSD (Setaram Setsys Eco Synchronous thermal analyzer).

5. Results

5.1. XRD and SEM

The XRD pattern of the $Mg_{30}Zn_{30}Sn_{30}Sr_5Bi_5$ alloy is shown in Figure 8. It can be clearly seen that the alloy consists of multiple phases, included Mg_3Bi_2, MgSnSr, Mg_2Sn, Mg_4Sr, $Mg_{38}Sr_9$, and MgZn. The SEM image of as-cast $Mg_{30}Zn_{30}Sn_{30}Sr_5Bi_5$ alloy is shown in Figure 9.

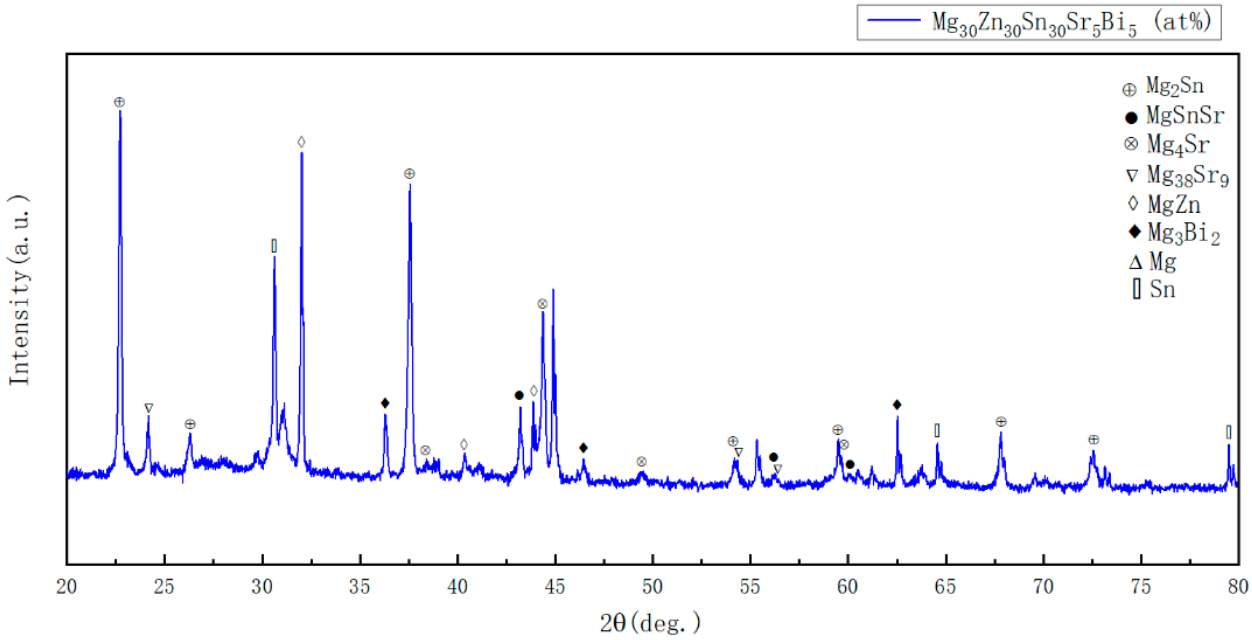

Figure 8. The XRD patterns of the as-cast $Mg_{30}Zn_{30}Sn_{30}Sr_5Bi_5$ alloy.

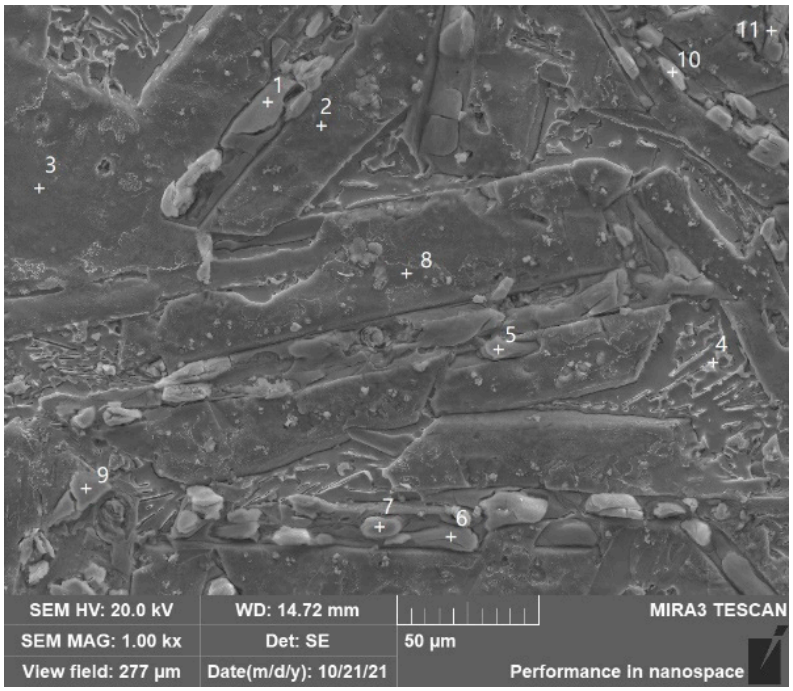

Figure 9. The SEM image of the as-cast $Mg_{30}Zn_{30}Sn_{30}Sr_5Bi_5$ alloy.

The combined XRD and SEM analysis shows that the structure of the new material $Mg_{30}Zn_{30}Sn_{30}Sr_5Bi_5$ (at.%) is very complex: there are multiple crystal systems and the types of space groups are also diverse. The energy spectrum analysis includes a total of 11 spectrogram analysis points. The analysis results show that the Mg element as a matrix element meets the design requirements of a nearly uniform distribution in the alloy.

The atomic percentages of four positions, spectrum1, spectrum5, spectrum6, and spectrum9, are analogous. In these positions, the atomic percentage of Bi is the highest. The analysis shows there are two phases; Mg_3Bi_2 (Crystal system: Hexagonal, Space group: P-3m1, Space group number: 164) and MgSnSr (Crystal system: Orthorhombic, Space group: Pnma, Space group number: 62) represent the existence of the phases. Among these, the MgSnSr phase is rod-shaped. When the content of the Sr element increases, the formation trend of the MgSnSr phase is gradually higher than that of the Mg_2Sn phase, and the MgSnSr phase has a dispersion strengthening effect, which improves the mechanical properties of the alloy at room temperature. The Mg_3Bi_2 compound has good thermal stability and creep resistance, and a good precipitation strengthening effect can be obtained by heat treatment. In the four positions, spectrum2, spectrum3, spectrum8, and spectrum11, the atomic percentages of the main element Mg and Sn are both close to 2:1, and the other elements in these four positions rarely approach 0. Thus, the four positions can be considered as a single phase of Mg_2Sn (Crystal system: Cubic, Space group: Fm-3m, Space group number: 225). The Mg_2Sn compound can effectively improve the amorphous formation of Mg alloy. The main phase in spectrum7 is Mg4Sr (Crystal system: Hexagonal, Space group: P63/mmc, Space group number: 194). Because the Mg4Sr phase structure refinement disperses the distribution, it improves the properties of Mg-based and Sr-based alloys, lowering the melting temperature and enthalpy. The analysis results of spectrum10 shows that after Sr is added to Mg, $Mg_{38}Sr_9$ (Crystal system: Hexagonal, Space group: P63/mmc, Space group number: 194) phase will be formed. The phase leads to easier solidification of the Mg-based alloys because the growth of grains is restricted. The contents of Mg, Zn, and Sn in spectrum4 are relatively high, whereas the contents of Sr and Bi are extremely low. According to the existing research data, this region can be regarded as the dependent existence of the MgZn phase and Mg_2Sn phase, and most of the MgZn phase should exist in the eutectic mode of the α-Mg+MgZn phase. In addition, since the constituent elements of the new material all have strong oxidizability, there are more

oxygen elements in the alloy, and the oxides of multiple elements also appear in the alloy, such as MgO, $ZnSnO_3$, and other phases. The presence of the Sn element is also similar to that in the simulation result. The Sn element precipitates out of solid solution at room temperature and exists as an element. The percentage mentioned in the paragraph refers to the one in Table 1.

Table 1. SEM energy spectrum analysis results.

	Mg at.%	Zn at.%	Sn at.%	Sr at.%	Bi at.%	O at.%
Spectrogram 1	9.86	1.65	2.31	2.35	20.39	63.43
Spectrogram 2	50.60	0.25	27.34	0.34	0.08	21.39
Spectrogram 3	41.94	0.29	39.48	0.18	0.36	17.75
Spectrogram 4	9.22	21.95	34.86	0.65	0.27	33.06
Spectrogram 5	10.17	0.74	2.37	2.34	22.37	62.01
Spectrogram 6	10.59	1.12	3.51	3.72	20.21	60.85
Spectrogram 7	12.29	1.44	5.87	3.50	17.60	59.30
Spectrogram 8	50.86	0.15	27.03	0.28	0.12	21.55
Spectrogram 9	9.24	1.34	2.48	2.33	18.52	66.08
Spectrogram 10	13.29	1.37	3.29	3.00	13.92	65.14
Spectrogram 11	39.09	0.65	25.51	0.30	0.07	34.38

5.2. Mechanical Properties

The melting point of the $Mg_{30}Zn_{30}Sn_{30}Sr_5Bi_5$ (at.%) was tested by PSD (sample mass 43.32 mg, test temperature range is 0–800 °C). In the range of 390–430 °C, the alloy was in a state of heat absorption and exothermic equilibrium, and the curve shows a horizontal state. In the range of 190–200 °C, the heat flow peak appears in the curve. Combined with the simulation analysis, and XRD and SEM analyses, a large amount of Sn is precipitated in the simple form at this temperature range. In other temperature ranges, the heat flow of specimens increased with the increase in equipment temperature without obvious fluctuation. The test results of the different temperature capacities of the vacuum melting furnace show that the melting point of the material is about 420 °C. This is obviously lower than the melting point value of the common Mg alloys, which is above 600 °C. Considering the requirements of the casting process, it is more advantageous.

The elastic modulus of $Mg_{30}Zn_{30}Sn_{30}Sr_5Bi_5$ (at.%) is 17.98 GPa, which is very similar to that of human bones. The density of $Mg_{30}Zn_{30}Sn_{30}Sr_5Bi_5$ (at.%) is 4.47 g/cm^3.

The density, elastic modulus, and compressive yield strength of $Mg_{30}Zn_{30}Sn_{30}Sr_5Bi_5$ (at.%) are compared with the performance of human bone and common biological implant materials in Table 2.

Table 2. The performance comparison between human bone, common biological implant materials [52], and $Mg_{30}Zn_{30}Sn_{30}Sr_5Bi_5$ (at.%).

Properties	Natural Bone	Magnesium	Ti Alloy	Co-Cr Alloy	Stainless Steel	$Mg_{30}Zn_{30}Sn_{30}Sr_5Bi_5$
Density	1.8–2.1	1.74–2.0	4.4–4.5	8.3–9.2	7.9–8.1	4.47
Elastic modulus	3–20	41–45	110–117	230	189–205	17.98
Compressive yield strength	130–180	65–100	758–1117	450–1000	170–310	192.84

Unit: density: g·cm^{-3}, elastic modulus: GPa, compressive yield strength: MPa.

In addition, the hardness test results of $Mg_{30}Zn_{30}Sn_{30}Sr_5Bi_5$ (at.%) showed that the mixing of various components was not the most uniform state because the material was prepared by natural cooling under the protection of argon after melting, and there was no stirring. Therefore, the hardness values at different positions fluctuated to a certain extent, and the measured values ranged from 100 to 250 HV. The maximum hardness value was 249 HV.

In this study, measurement instruments used included: German Zeiss Gemini 300 field emission scanning electron microscope, OXFORD x-max 50 mm^2 type X-ray energy spectrometer, X 'pert Powder type X-ray diffractometer, Setaram Setsys Evo synchronous

thermal analyzer, WDW-100 electronic universal testing machine, and HV-1000 microhardness tester.

6. Conclusions

The melting point of $Mg_{30}Zn_{30}Sn_{30}Sr_5Bi_5$ (at.%) is about 420 °C, which was proven by the PSD test; this numerical value is lower than the melting point of existing Mg alloys. From the perspective of casting material processing, it has a more significant advantage: the elastic modulus of the Mg is 17.98 GPa, which is closer to the elastic modulus value of human bones, and the alloy can avoid the problem of stress shielding. Although the density of $Mg_{30}Zn_{30}Sn_{30}Sr_5Bi_5$ (at%) is 4.47 g/cm^3, which is higher than the value of 1.74–2.0 g/cm^3 of existing Mg-based biomaterials [53], it is lower than the density values of other biomaterials. Because of its multi-element structural characteristics, the density of A can be adjusted by the variation in the elements' atomic percentages. In the research process, the author used an exhaustive method to establish a simple calculation model, in which the calculation condition was set as: $Mg_aZn_bSn_cSr_dBi_e$ (at.%), and $30 \leq a \leq 35$, $5 \leq b \leq 30$, $5 \leq c \leq 30$, $5 \leq d \leq 30$, $5 \leq e \leq 30$, and $a + b + c + d + e = 100$. The final result shows that, when the atomic percentage of various elements is 30:29:7:29:5, the material can obtain a minimum value of 3.76 g/cm^3. This proportioning scheme can be further studied and demonstrated in subsequent studies.

Based on the purpose of the current material research, subsequent research should mainly be undertaken on the following aspects: (a). Mg-based biomaterials are used as excellent degradable biological implant materials, and the study of corrosion resistance has recently been a popular research topic. As a new biomaterial, the study of the corrosion resistance of $Mg_aZn_bSn_cSr_dBi_e$ is required. (b). According to the current research results of the prepared materials, the distribution of internal components of materials is not uniform, which leads to some fluctuations in the analysis results of material properties. (c). As a kind of biomaterial, some of the alloy's mechanical properties meet the use requirements of biomaterials, but its properties still need to be further adjusted from the perspective of processing. (d). In the current research, laser treatment on the surface of the material can significantly improve the distribution of the internal crystal system, and the thinning effect is obvious. The performance changes caused by the laser treatment will be further promoted in subsequent research.

7. Patents

The material A designed in this study was the subject of an invention patent application formally filed with the Chinese Patent Office, and has received a patent application acceptance notice. Patent Application No.: 202111500334.1

Author Contributions: Conceptualization, B.M. and D.J.; methodology, B.M.; software, B.M.; validation, B.M. and D.J.; formal analysis, B.M.; investigation, B.M. and D.J.; resources, B.M. and Q.L.; data curation, B.M. and Q.L.; writing—original draft preparation, B.M.; writing—review and editing, D.J. and B.M.; visualization, B.M.; supervision, D.J.; project administration, B.M., D.J. and Q.L. All authors have read and agreed to the published version of the manuscript.

Funding: This research received no external funding.

Institutional Review Board Statement: Not applicable.

Informed Consent Statement: Not applicable.

Data Availability Statement: Not applicable.

Acknowledgments: We sincerely thank Zhongnuo Advanced Material (Beijing) Technology Co., Limited for the material preparation. We sincerely thank Beijing Wuzhouy—Anghe & Partners (Chuncheng LIU, Patent attorney, Civil Litigation Attorney, Partner Beijing Wuzhouy—Anghe & Partners. Address: A1908, Vantone New World, No.2, Fuchengmenwai Avenue. Xicheng District, Beijing, China. Post Code: 100037. Tel.: +86-10-6801-6746. Mobile: 18612213819. Fax: +86-10-6801-

6046. Email: liuchuncheng@wzyhip.com. Web: www.wzyhip.com 12 September 2021) for patent application (CN 114164370 A).

Conflicts of Interest: The authors declare no conflict of interest.

References

1. Black, J. *Biological Performance of Materials: Fundamentals of Biocompatibility*; CRO Press: Boca Raton, FL, USA, 2005.
2. Fini, M.; Nicoli Aldini, N.; Torricelli, P.; Giavaresi, G.; Borsari, V.; Lenger, H.; Bernauer, J.; Giardino, R.; Chiesa, R.; Cigada, A. A new austenitic stainless steel with engligible nickel content: An in vitro and in vivo comparative investigation. *Biomaterials* **2003**, *24*, 4929–4939. [CrossRef]
3. Khandan, A.; Abdellahi, M.; Barenji, R.V.; Ozada, N.; Karamian, E. Introducing natural hydroxyapatite-diopside (NHA-Di) nano-bioceramic coating. *Ceram. Int.* **2015**, *41*, 12355–12363. [CrossRef]
4. MA, X.M.; YANG, Y.J.; SUN, W. Current Research Progress of β-type Ti-Nb-Ta-Zr Alloys for Biomedical Applications. *Mater. Rep.* **2008**, *8*, 344–347.
5. Niinomi, M. Mechanical properties of biomedical titanium alloys. *Mater. Sci. Eng. A* **1998**, *243*, 231. [CrossRef]
6. Wang, Y.F.; He, L.; Guo, W. Research and Application of Medical Titanium Alloy. *Titan. Ind. Prog.* **2015**, *32*, 1–6.
7. Tan, L.; Yu, X.; Wan, P.; Yang, K. Biodegradable materials for bone repairs: A review. *J. Master. Sci. Technol.* **2013**, *29*, 503–513. [CrossRef]
8. Zhang, X.B.; Ba, Z.X.; Wang, Q.; Wu, Y.J.; Wang, Z.Z.; Wang, Q. Uniform corrosion behavior of GZ51K alloy with long period stacking ordered structure for biomedical application. *Corros. Sci.* **2014**, *88*, 1–5. [CrossRef]
9. Zheng, Y.F.; Gu, X.N.; Witte, F. Biodegradable Metals. *Mater Sci. Eng.* **2014**, *77*, 1–34. [CrossRef]
10. Lin, X.; Yang, X.M.; Tan, L.L.; Li, M.; Wang, X.; Zhang, Y.; Yang, K.; Hua, Z.Q.; Qiu, J.H. In vitro degradation and biocompatibility of a strontium-containing micro-arc oxidation coating on the biodegradable ZK60 magnesium alloy. *Appl. Surf. Sci.* **2014**, *288*, 718–726. [CrossRef]
11. Zheng, Y.; Li, Y.; Chen, J.H.; Zou, Z.Y. Effects of tensile and compressive deformation on corrosion behaviour of a Mg–Zn alloy. *Corros. Sci.* **2015**, *90*, 445–450. [CrossRef]
12. Chen, Q.Z.; Thouas, G.A. Metallic implant biomaterials. *Mater. Sci. Eng. R* **2015**, *87*, 1–57. [CrossRef]
13. Seong, J.W.; Kim, W.J. Development of biodegradable Mg–Ca alloy sheets with enhanced strength and corrosion properties through the refinement and uniform dispersion of the Mg2Ca phase by high-ratio differential speed rolling. *Acta Biomater.* **2015**, *11*, 531–542. [CrossRef] [PubMed]
14. Liu, J.; Zheng, Y.; Bi, Y.Z.; Li, Y.; Zheng, Y.F. Improved cytocompatibility of Mg-1Ca alloy modified by Zn ion implantation and deposition. *Mater. Lett.* **2017**, *205*, 87–89. [CrossRef]
15. Zberg, B.; Uggowitzer, P.J.; Löffler, J.F. Mg ZnCa glasses without clinically observablehydrogen evolution for biodegradable implants. *Nat. Mater.* **2009**, *8*, 887–891. [CrossRef] [PubMed]
16. Gu, X.; Zheng, Y.; Zhong, S.; Xi, T.; Wang, J.; Wang, W. Corrosion of, and cellular responses to Mg-Zn-Ca bulkmetallic glasses. *Biomaterials* **2010**, *31*, 1093–1103. [CrossRef]
17. Witte, F.; Reifenrath, J.; Muller, P.; Crostack, H.-A.; Nellesen, J.; Bach, F.; Bormann, D.; Rudert, M. Cartilage Repair on Magnesium Scaffolds Used as a Subchondral Bone Replacement. *Mater. Und Werkst.* **2006**, *37*, 504–508. [CrossRef]
18. Waizy, H.; Dickmann, J.; Weizbauer, A.; Reifenrath, J.; Bartsch, I.; Neubert, V.; Schavan, R.; Windhagen, H. In vivo study of a biodegradable orthopedic screw (MgYREZr-alloy) in a rabbit model for up to 12 months. *J. Biomater. Appl.* **2013**, *28*, 667. [CrossRef]
19. Dickmann, J.; Bauer, S.; Weizbauer, A.; Willbold, E.; Windhagen, H.; Helmecke, P.; Lucas, A.; Reifenrath, J.; Nolte, I.; Ezechieli, M. Examination of a biodegradable magnesium screw for the reconstruction of the anterior cruciate ligament: A pilot in vivo study in rabbits. *Mater. Sci. Eng. C* **2016**, *59*, 1100–1109. [CrossRef]
20. Windhagen, H.; Radtke, K.; Weizbauer, A.; Diekmann, J.; Noll, Y.; Kreimeyer, U.; Schavan, R.; Stukenborg-Colsman, C.; Waizy, H. Biodegradable magnesium-based screw clinically equivalent to titanium screw in hallux valgus surgery: Short term results of the first prospective, randomized, controlled clinical pilot study. *Biomed. Eng. Online* **2013**, *12*, 62. [CrossRef]
21. Kenan, C.; Chuanbin, G. Research progress on biodegradable medial magnesium-based materials. *Int. J. Stomatol.* **2021**, *48*, 322–328.
22. Kumar, A.; Pandey, P.M. Development of Mg based biomaterial with improved mechanical degradation properties using powder metallurgy. *J. Magnes. Alloy.* **2020**, *8*, 883–898. [CrossRef]
23. Frost, H.M. A 2003 Update of Bone Physiology and Wolff's Law for Clinicians. *Angle Orthod.* **2004**, *74*, 3–15.
24. Raffa, M.L.; VNguyen, H.; Hernigou, P.; Flouzat-Lachaniette, C.H.; Haiat, G. Stress Shielding at the bone-implant interface: Influence of surface roughness and of the bone-implant contact ration. *Orthop Res.* **2021**, *39*, 1174–1183. [CrossRef] [PubMed]
25. Zhang, Y. Microstructure, Mechanical Properties and the Mechanism of Film Layer Formation and Degradation of Mg Alloys Containing Ca and Nd. Ph.D. Thesis, School of Materials Science and Engineering, University of Science and Technology, Beijing, China, 2019.
26. Yeh, J.W.; Chen, S.K.; Lin, S.J.; Gan, J.Y.; Chin, T.S.; Shun, T.T.; Tsau, C.H.; Chang, S.Y. Nanostructured high-entropy alloys with multiple principal elements: Novel alloy design concepts and outcomes. *Adv. Eng. Mater.* **2004**, *6*, 299–303. [CrossRef]

27. Cantor, B.; Knight, P.; Chang, I.T.H.; Vincent, A.J.B. Microstructural development in equiatomic multicomponent alloy. *Mater. Sci. Eng. A* **2004**, *375–377*, 213–218. [CrossRef]
28. Senkov, O.N.; Wilks, G.B.; Miracle, D.B.; Chuang, C.P.; Liaw, P.K. Refractory high-entropy alloys. *Intermetallics* **2010**, *18*, 1758–1765. [CrossRef]
29. Zhang, C.; Gao, M.C.; Yeh, J.W.; Liaw, P.K.; Zhang, Y. *High-Entropy Alloys—Fundamentals and Applications*; Springer International Publishing: Cham, Switzerland, 2016.
30. Toda-Caraballo, I.; Rivera-Diaz-del-Castillo, P.E. Modelling solid solution hardening in high entropy alloys. *Acta Mater.* **2015**, *85*, 14–23. [CrossRef]
31. Srivatsan, T.S.; Gupta, M. *High Entropy Alloys—Innovations, Advances, and Applications*, 1st ed.; CRC Press—Tayior & Francis Group: Boca Raton, FL, USA, 2020.
32. Yin, B.; Curtin, W.A. First-principles-based Prediction of Yield Strength in the RhIrPdPtNiCu High-Entropy Alloy. *NPJ Comput. Mater.* **2019**, *5*, 14.
33. Kasem, M.R.; Hoshi, K.; Jha, R.; Katsuno, M.; Yamashita, A.; Goto, Y.; Matsuda, T.D.; Aoki, Y.; Mizuguchi, Y. Superconducting Properties of High-entropy-alloy Tellurides M-Te (M: Ag, In, Cd, Sn, Sb, Pb, Bi) with a NaCl-type Structure. *Appl. Phys. Express* **2020**, *13*, 033001. [CrossRef]
34. Shivam, V.; Sanjana, V.; Mukhopadhyay, N.K. Phase Evolution and Thermal Stability of Mechanically Alloyed AlCrFeCoNiZn High-Entropy Alloy. *Trans. Indian Inst. Met.* **2020**, *73*, 821–830. [CrossRef]
35. Poletti, M.G.; Branz, S.; Fiore, G.; Szost, B.A.; Crichton, W.A.; Battezzati, L. Equilibrium High Entropy Phases in X-NbTaTiZr (X = Al, V, Cr and Sn) Multiprincipal Component Alloys. *J. Alloy. Compd.* **2016**, *655*, 139–146. [CrossRef]
36. Singh, N.; Shadangi, Y.; Mukhopadhyay, N.K. Phase Evolution and Thermal Stability of Low-Density MgAlSiCrFe High-Entropy Alloy Processed Through Mechanical Alloying. *Trans. Indian Inst. Met.* **2020**, *73*, 2377–2386. [CrossRef]
37. Sandar, T.K.; Manoj, G. Microstructural Evolution in MgAlLiZnCaY and MgAlLiZnCaCu Multicomponent High Entropy Alloys. *Mater. Sci. Forum* **2018**, *928*, 183–187.
38. Zong, X.; Zhang, J.; Liu, W.; Zhang, Y.; You, Z.; Xu, C. Corrosion Behaviors of Long-Period Stacking Ordered Structure in Mg Alloys Used in Biomaterials: A Review. *Adv. Eng. Mater.* **2018**, *20*, 1800017. [CrossRef]
39. Liu, Y.; Zheng, Y.; Chen, X.H.; Yang, J.A.; Pan, H.; Chen, D.; Wang, L.; Zhang, J.; Zhu, D.; Wu, S.; et al. Fundamental Theory of Biodegradable Metals-Definition, Criteria, and Design. *Adv. Funct. Mater.* **2019**, *29*, 1805402. [CrossRef]
40. Meng, X.; Jiang, Z.; Zhu, S.; Guan, S. Effetcs of Sr Addition on Microstructure, Mechanical and Corrosion Properties of Biodegradable Mg-Zn-Ca Alloy. *J. Alloy. Compd.* **2020**, *838*, 155611. [CrossRef]
41. Chen, K.; Xie, X.; Tang, H.; Sun, H.; Qin, L.; Zheng, Y.; Gu, X.; Fan, Y. In Vitro and in Vivo Degradation Behavior of Mg-2Sr-Ca and Mg-2Sr-Zn alloys. *Bioact. Mater.* **2020**, *5*, 275–285. [CrossRef]
42. Sheng, L.; Du, B.; Hu, Z.; Qiao, Y.; Xiao, Z.; Wang, B.; Xu, D.; Zheng, Y.; Xi, T. Effects of Annealing Treatment on Microstructure and Tensile Behavior of the Mg-Zn-Y-Nd Alloy. *J Magnes Alloys.* **2020**, *8*, 601–613. [CrossRef]
43. Yang, K.; Zhou, C.; Fan, H.; Fan, Y.; Jiang, Q.; Song, P.; Fan, H.; Chen, Y.; Zhang, X. Bio-functional Design, Application and Trends in Metallic Biomaterials. *Int. J. Mol. Sci.* **2018**, *19*, 24. [CrossRef]
44. Ostrakhovitch, E.A.; Cherian, M.G. Tin. In *Handbook on the Toxicology of Metals*, 4th ed.; Nordberg, G.F., Fowler, B.A., Nordberg, M., Friberg, L.T., Eds.; Elsevier: London, UK, 2015; Chapter 42; pp. 839–859.
45. Pouria, A.; Bandegani, H.; Pourbaghi-Masouleh, M.; Hesaraki, S.; Alizadeh, M. Physicochemical Properties and Cellular Responses of Strontium-Doped Gypsum Biomaterials. *Bioinorg. Chem. Appl.* **2012**, *2012*, 976495. [CrossRef]
46. Skerfving, S.; Bergdahl, I.A. Lead. In *Handbook on the Toxicology of Metals*, 4th ed.; Nordberg, G.F., Fowler, B.A., Nordberg, M., Friberg, L.T., Eds.; Elsevier: London, UK, 2015; Chapter 31; pp. 599–643.
47. Ren, W.L.; Li, Q.A.; Shi, Y.J. Effect of Bi on microstructure and mechanical properties of AZ81 magnesium alloy. *Rare Met. Cem. Carbides* **2010**, *38*, 34–37.
48. Nordberg, G.F.; Fowler, B.A.; Nordberg, M.; Friberg, L. *Handbook on the Toxicology of Metals*, 3rd ed.; Academic Press: Burlington, FA, USA, 2007; Chapter 22; pp. 433–443.
49. Chen, G.; Fan, P.G.; Peng, X.D.; Cao, P.J.; Cai, W. Effect of Sr addition on the microstructure and the properties of AZ91 magnesium alloy. *Light Alloy. Processing Technol.* **2008**, *36*, 15–18.
50. Qin, W.; Kolooshani, A.; Kolahdooz, A.; Saber-Samandari, S.; Khazaei, S.; Khandan, A.; Ren, F.; Toghraie, D. Coating the magnesium implants with reinforced nanocomposite nanoparticles for use in orthopedic applications. *Colloids Surf. A Physicochem. Eng. Aspects.* **2021**, *621*, 126581. [CrossRef]
51. Karamian, E.; Motamedi, M.R.K.; Khandan, A.; Soltani, P.; Maghsoudi, S. An in virto evaluation of novel NHA/zircon plasma coating on 316L stainless steel dental implant. *Prog. Nat. Sci. Mater. Int.* **2014**, *24*, 150–156. [CrossRef]
52. Guangyin, Y.; Jia, Z.; Wenjiang, D. Research Progress of Mg-Based Alloys as Degradable Biomedical Materials. *Mater. China* **2011**, *30*, 44–50.
53. Gu, X.N.; Zhou, W.R.; Zheng, Y.F.; Cheng, Y.; Wei, S.C.; Zhong, S.P.; Xi, T.F.; Chen, L.J. Corrosion fatigue behaviors of two biomedical Mg alloys—AZ91D and WE43—In simulated body fluid. *Acta Biomater.* **2010**, *5*, 4605–4613. [CrossRef]